Near-field coupling of a levitated nanoparticle to a photonic crystal cavity: supplementary material

LORENZO MAGRINI[1], RICHARD A. NORTE[2], RALF RIEDINGER[1], IGOR MARINKOVIĆ[2], DAVID GRASS[1], UROŠ DELIĆ[1], SIMON GRÖBLACHER[2,3], SUNGKUN HONG[1,4], AND MARKUS ASPELMEYER[1,5]

[1] *Vienna Center for Quantum Science and Technology (VCQ), Faculty of Physics, University of Vienna, A-1090 Vienna, Austria*
[2] *Kavli Institute of Nanoscience, Delft University of Technology, 2628CJ Delft, The Netherlands*
[3] *Corresponding author: s.groeblacher@tudelft.nl*
[4] *Corresponding author: sungkun.hong@univie.ac.at*
[5] *Corresponding author: markus.aspelmeyer@univie.ac.at*

Published 13 December 2018

This document provides supplementary information to "Near-field coupling of a lev-itated nanoparticle to a photonic crystal cavity," https://doi.org/10.1364/OPTICA.5.001597.

1. CAVITY AND FIBER FABRICATION

Photonic crystal nanobeam patterns are exposed into a resist layer, on samples consisting of 350 nm films of LPCVD silicon nitride (SiN) deposited on Si substrates, using electron-beam lithography. We use a CHF_3/O_2 directional plasma etch to transfer arrays of nanobeam structures into the SiN film. The surface is thoroughly cleaned using a (4:1) pirahna solution and the chip then dipped into in diluted hydrofluoric acid (HF) to remove oxidation from the exposed silicon surfaces. The SiN devices are released from the substrate using a SF_6 plasma release. This method allows us to produce very clean and smooth surfaces with high yield. The nanobeams are designed to taper down into a thin bridge connecting it to the substrate (left side in Fig. S1(a) and (b)). This allows us to break the nanobeams off the substrate using a tapered fiber. These fibers are made by cleaving and stripping Corning SMF28 optical fibers and pulling them from a container of HF solution at a speed of 0.2 μm/s for 70 minutes using computer controlled motors. A small amount of o-xylene is used as a thin protective layer on the surface of the HF in order to prevent HF vapor from etching (and roughening) other parts of the fiber as it is pulled from the beaker [1].

2. TRANSFER OF THE PHOTONIC CRYSTAL CAVITY TO THE TAPERED FIBER

We image the tapered fiber clamped to its holder using an optical 50x microscope objective with a long working distance. The chip with arrays of the photonic crystal cavities is placed on

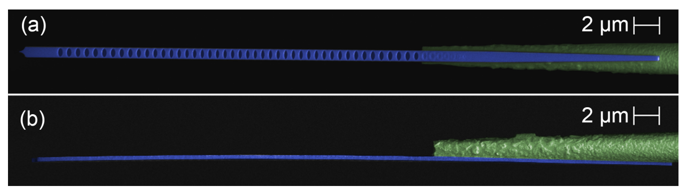

Fig. S1. Scanning electron microscope (SEM) images of a device. Shown are top (a) and side (b) views of the photonic crystal cavity (blue) and the tapered fiber (green) assembly used in the experiments presented in the main text. The roughness of the tapered fiber is mitigated by UV glue coating, which improves the contact to the cavity and a stronger van der Waals adhesion.

a translational stage below the fiber. By controlling the chip position we can now move the fiber tip into contact with the tapered end of the photonic crystal cavity. Once a cavity with good resonance, coupling and optical Q is found, we break it off the chip by forcing the fiber against it. In most cases, the cavity remains on the fiber due to attractive van der Waals force. The violent cavity lift-off step, however, causes a displacement of the cavity on the fiber such that the light coupling efficiency between the two is reduced. Readjustment of the alignment is then carried out with the help of a tungsten tip placed perpendicular to the fiber on a separate stage. Although the coupling can be partially restored, we found that the full recovery of the coupling efficiency is extremely challenging due to yet limited control over the overlap length of the two structures after lift-off. This results in a relatively low yield in obtaining high efficiency fiber-cavity assemblies. For this reason, the present work was carried out with a $\eta_{cav} = 0.32$, while no fundamental issue will prevent us from being more selective in choosing assemblies with higher efficiencies.

Due to the HF tapering, the fiber surface is quite rough [1] and in order to increase the contact surface to the cavity and improve the connection strength, we dip the tapered fiber into UV glue and cure it before picking up the device. This results in a strong bond which does not affect the coupling efficiency and greatly reduces the chances to lose one of the photonic crystal cavities while transferring it into the vacuum chamber.

3. PARTICLE LOADING

We load the nanoparticles into the tweezer trap at room pressure, keeping the cavity in vacuum in a separate chamber connected to the main chamber through a load lock valve. Once the particle is trapped and the main chamber is evacuated to around 1 mbar, we move the cavity positioner onto its holder in proximity to the trapping objective. Imaging through the trapping objective allows us to precisely control its position. Using a dichroic mirror, we can separate the trapping laser from the green ($\lambda_{im} = 532$ nm) illumination light which is used to image the particle and the cavity at the same time. In order to obtain a well aligned trapping beam during the experiment, we tilt the last mirror, thereby moving the particle above the center of the objective field of view and center the cavity by controlling its nanopositioner (Fig. S2). Once the cavity is in place, we move

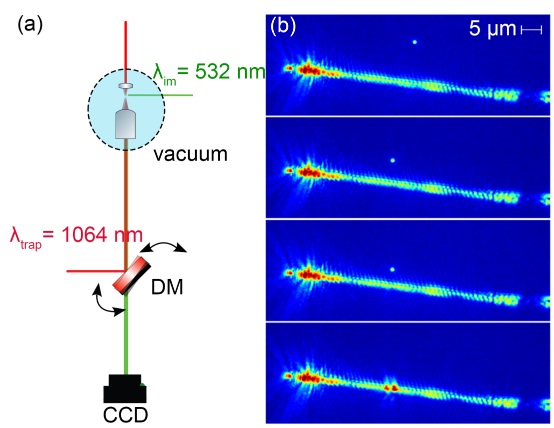

Fig. S2. Position control of the levitated nanoparticle. (a) Position control of the trapped particle is achieved by tilting of the dicroic mirror (DM) just before the opbjective. As also shown by Diehl *et al.* [2], the trapping objective is also used to image the particle and photonic crystal cavity by collection of scattered $\lambda_{im} = 532$ nm light coming from the side. (b) Scattering images of the nanoparticle approaching the photonic crystal cavity as the trapping beam is tilted. When the particle is in front of the cavity, not perfect extinction of the reflected trapping light causes the camera to saturate hiding the particle.

the trapped particle in front of the cavity by tilting the mirror back into its original position. The cavity output signal allows us to measure the coupling strength and particle frequency, determining the particle position inside the lattice: if the particle is measured to be in the second or third lobe away from the cavity, we tilt the mirror away again, move the cavity closer into the microscope's focus and repeat the procedure until we observe large optomechanical coupling (Fig. 4 in the main text). After the particle is positioned in the first lobe, we define the lateral positioning in the cavity field, by moving the cavity itself in steps of ~ 10 nm.

4. DETECTION EFFICIENCY AND SENSITIVITY

We pump the cavity with 260 nW laser power, and the output field is guided to homodyne detection. The total detection efficiency is $\eta = \eta_{loss}\eta_q\kappa_{in}/\kappa = 0.09$, with $\kappa_{in}/\kappa = 0.5$ the ratio of cavity input to total energy decay rate, $\eta_{loss} = 0.22$ the transmission of all other optical components, and $\eta_q = 0.85$ the detector quantum efficiency at $\lambda = 1550$ nm. In contrast, for far-field detection, the trapping beam is re-collimated by a secondary objective together with the particle's scattered light and directed to a balanced detector where the common laser noise is cancelled. It is attenuated to typically 1 mW in order to stay in the linear regime of the photodetector. In this case the detection efficiency of the particle scattered light is estimated to be below $\eta_F \sim 10^{-3}$ [3].

To compare the sensitivities of both detection schemes, we first acquire the power spectral densities of each methods in the presence (Fig. S3), as well as in the absence of the particle (not shown). The signal-to-noise ratio (SNR) can then be extracted by taking the ratio between integrated powers of these two spectra. SNR can be expressed as $\sqrt{\mathrm{SNR}} \propto \sqrt{\dot{n}_{det}}\chi$, where $\dot{n}_{det}$ is the rate of detected photons and χ is the single-photon measurement strength. This gives us an estimate of the ratio

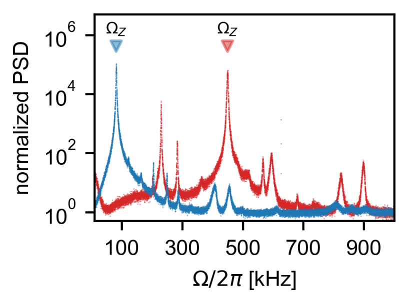

Fig. S3. Measured power spectral densities of a particle's motion via far-field (blue) and cavity near-field (red) detection. The optical power detected in the far-field case is of about 1 mW, while in the case of cavity detection, the signal reaching the homodyne detection is of less than 60 nW. The significant difference in mechanical frequencies is due do the formation of a standing wave trap in the presence of the cavity device.

of single-photon measurement strengths for the two detection schemes, $\chi_0/\chi_F \sim 10^2$, with χ_0 and χ_F the near- and far-field single-photon measurement strengths respectively.

χ_0 can be independently calculated from $\chi_0 = 2g_0/\kappa = 5.2 \times 10^{-6}$. We note that it is already very close to the maximally allowed far-field single-photon measurement strength $\chi_F^{max} = 4\pi x_{\mathrm{ZPF}}/\lambda_{trap} = 2.0 \times 10^{-5}$ [4]. It also shows that the large χ_0/χ_F ratio in the experiment is a result of the drastic difference between the near- and far-field detection efficiencies.

The detection efficiency can be further improved by reducing optical losses $\eta_{loss} = \eta_{cav}\eta_{path}$, where η_{cav} is the coupling efficiency between the photonic crystal's waveguide and the tapered fiber and η_{path} is the total transmission efficiency of the rest of the optical path. Currently, η_{path} includes the loss of many fiber connectors, which can be replaced by almost lossless splices. At the same time, while all measurements were performed with a device with $\eta_{cav} = 0.32$, we successively were able to pick up a device maintaining and efficiency of $\eta_{cav} = 0.97$, similarly to what shown by Burek *et al.* [1].

5. CALIBRATION OF THE OPTOMECHANICAL COUPLING

The calibration of the frequency shift per displacement $G = d\omega_{cav}/dx$ was carried out by evaluating the measured power spectral densities $S_W(\Omega)$ compared to the measured shot-noise level S_W^{sn}. Using the known Poissonian statistics governing the photon shot noise, one can estimate the amount of detected photons and their contribution to the noise level. This allows is to calibrate the signal in units of photons. The position spectral density of the particle is that of a damped harmonic oscillator subject to a stochastic Langevin force

$$S_{xx}(\Omega) = 2\left\langle x^2 \right\rangle \frac{\Gamma\Omega_m^2}{(\Omega_m^2 - \Omega^2)^2 + \Gamma^2\Omega^2}, \tag{S1}$$

where the particle is in thermal equilibrium with its bath $\langle x^2 \rangle = k_B T/m\Omega_m^2$. The fluctuations of the cavity resonance are related to the particles position through $G = d\omega_{cav}/dx$

$$S_{\omega\omega}(\Omega) = G^2 S_{xx}(\Omega). \tag{S2}$$

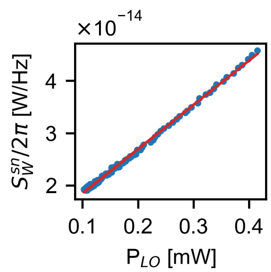

Fig. S4. Shot-noise power dependence. Linear dependence of the shot-noise level as a function of optical power of the local oscillator.

Considering the optical annihilation operator $\hat{a}$, it is convenient to make use of the input-output formalism in order to evaluate the mechanically induced noise [5]. The cavitiy field the reads

$$\hat{a} = \frac{\sqrt{\kappa_{in}}\hat{a}_{in} + \sqrt{\kappa_0}\hat{a}_0}{-i\Delta + \frac{\kappa}{2}}, \tag{S3}$$

where κ_0 is the intrinsic cavity decay rate, $\Delta = \omega_L - \omega_{cav} + \delta\omega$ the detuning between the laser frequency ω_L and the cavity resonance ω_{cav}, $\delta\omega$ the mechanical induced frequency fluctuations, $\hat{a}_0$ and $\hat{a}_{in}$ the annihilation operators defining the environment vacuum and input field amplitudes respectively. The output field $\hat{a}_{out}$ is given by

$$\begin{aligned}\hat{a}_{out} &= \hat{a}_{in} - \sqrt{\kappa_{in}}\hat{a} \\ &= \hat{a}_{in} - \sqrt{\kappa_{in}}\left(\sqrt{\kappa_{in}}\hat{a}_{in} + \sqrt{\kappa_0}\hat{a}_0\right)\left(\frac{\kappa/2}{\Delta^2 + \left(\frac{\kappa}{2}\right)^2} + i\frac{\Delta}{\Delta^2 + \left(\frac{\kappa}{2}\right)^2}\right) \\ &\sim -i\frac{2\delta\omega}{\kappa}\hat{a}_{in} - i\frac{2\delta\omega}{\kappa}\hat{a}_0 - \hat{a}_0,\end{aligned} \tag{S4}$$

where the approximation arises when considering a resonant laser drive $\omega_L = \omega_{cav}$, and mechanical resonance fluctuations that are much smaller than the cavity linewidth $\Delta = \delta\omega \ll \kappa$. In addition, critical coupling $\kappa/2 = \kappa_{in} = \kappa_0$ is also assumed to further reduce the parameter space. Using Eq. (S4), considering a strong coherent input field $\hat{a}_{in} \to \hat{a}_{in} + \alpha_{in}$ with α_{in} real valued, the commutation relation $\left[\hat{a}(t), \hat{a}^\dagger(t+\tau)\right] = \delta(\tau)$, and defining the phase quadrature operator as $\hat{Y} = \hat{a}_{out} - \hat{a}_{out}^\dagger/(\sqrt{2}i)$, the phase quadrature spectral density can be computed:

$$\begin{aligned}S_{YY}(\Omega) &= \int_{-\infty}^{+\infty} d\tau\, e^{i\Omega\tau} \left\langle \hat{Y}(t+\tau)\hat{Y}(t) \right\rangle \\ &\sim 2\frac{4\bar{\alpha}_{in}^2}{\kappa^2} \int_{-\infty}^{+\infty} d\tau\, e^{i\Omega\tau} \left\langle \delta\omega(t+\tau)\delta\omega(t) \right\rangle + \frac{1}{2}\int_{-\infty}^{+\infty} d\tau\, e^{i\Omega\tau}\delta(\tau) \\ &= 2\frac{4\bar{\alpha}_{in}^2}{\kappa^2} S_{\omega\omega}(\Omega) + \frac{1}{2} = 2\bar{\alpha}_{in}^2 S_{\varphi\varphi}(\Omega) + \frac{1}{2}.\end{aligned} \tag{S5}$$

The output signal is then attenuated by optical losses η_{loss}, and amplified by a strong local oscillator of amplitude β_0 in a homodyne detection scheme. In addition, we consider the non unity quantum efficiency of the detectors yet as another attenuation channel η_q, affecting the expectation values of the field operator products ($\alpha_{in} \to \sqrt{\eta_{loss}}\sqrt{\eta_q}\alpha_{in},\ \beta_0 \to \sqrt{\eta_q}\beta_0$) [6]. At each detector the optical power spectral density is

$$S_{PP}(\Omega) = 4\eta_{loss}\eta_q^2 h^2\nu^2\bar{\alpha}_{in}^2\beta_0^2 S_{\varphi\varphi}(\Omega) + S_{PP}^{sn}, \tag{S6}$$

where $S_{PP}^{sn} = h^2\nu^2\eta_q\beta_0^2$ is the two-sided photon shot-noise level. When a photon is detected, it is converted into an electron current: $i(t) = n(t)e$, where $n(t)$ is the number of detected photons photons and e the electron charge. Non unity of the quantum efficiency of detectors has been already considered in Eq. (S6) as an effective optical loss [6]. Photo-currents from each detector are subtracted and the DC component as well as classical laser noise are cancelled. The current can then be amplified and converted into a voltage signal via the transimpedance amplifier $v(t) = g_t i_{AC}(t)$. It is now convenient to define the lossless optical power to voltage conversion factor as

$$G_{RF} = \frac{g_t\, e}{h\nu}. \tag{S7}$$

Finally, the measured two-sided power spectral density reads:

$$\begin{aligned}S_W(\Omega) &= \frac{G_{RF}^2}{R_L} 4 S_{PP}(\Omega) = \\ &\frac{G_{RF}^2}{R_L} 4\eta_q^2\eta_{loss}P_{in}P_{LO}\frac{4G^2}{\kappa^2}S_{xx}(\Omega) + S_W^{sn},\end{aligned} \tag{S8}$$

where $P_{in} = h^2\nu^2\bar{\alpha}_{in}^2$ ($P_{LO} = h^2\nu^2\beta_0^2$) is the cavity input (local oscillator) power, R_L is the input impedance of the measuring instrument, and $S_W^{sn} = G_{RF}^2\eta_q P_{LO}h\nu/R_L$ is the two-sided shot-noise level in the unit of W/Hz. The conversion factor G_{RF} can now be written in terms of measured quantities:

$$G_{RF} = \sqrt{\frac{S_W^{sn}R_L}{\eta_q P_{LO}h\nu}}. \tag{S9}$$

Substituting Eq. (S9) into Eq. (S8), we obtain

$$S_W(\Omega) = \frac{S_W^{sn}\eta_q}{h\nu}4\eta_{loss}P_{in}\frac{4G^2}{\kappa^2}S_{xx}(\Omega) + S_W^{sn}. \tag{S10}$$

The optomechanical coupling can now be derived by integrating the power spectral density

$$G = \sqrt{\frac{\int_{-\infty}^{+\infty} S_W(\Omega)\frac{d\Omega}{2\pi}}{\frac{k_B T}{m\Omega_m^2}} \frac{\kappa^2 h\nu}{S_W^{sn} 8\eta_{loss}\eta_q P_{in}}}. \tag{S11}$$

In Eq. (S11) the negative contribution arising from the shot-noise is neglected as it is orders of magnitude lower due to the large optomechanical coupling rate.

6. CAVITY HEATING

The cavity resonance strongly depends on heating, arising both from the optical field of the tweezer and the cavity pump field. Heating effects are particularly evident in vacuum, where heat dissipation is less efficient. The heating from the tweezer field results in a static frequency shift of the cavity, where the amount of the shift varies depending on the position of the cavity relative to the tweezer beam. We therefore scan the wavelength of the cavity pump laser at each position of the cavity (Fig. S5(a)) and set the laser on resonance, which is the optimal condition for homodyne readout of the motion. Heating arising from the cavity pump field strongly depends on the wavelength of the pump laser which defines the intra-cavity photon population, leading to a thermo-optic instability. These effects are visible when scanning the pump wavelength: the expected Lorentzian response in the reflected signal shows an asymmetry due to dynamic heating effects when the power is too high (Fig. S5(b)). We run the experiments with $P_{in} \sim 260$ nW ($n_{cav} \sim 800$), far below the input powers where a sizable deviation from the lorenzian line shape can be observed.

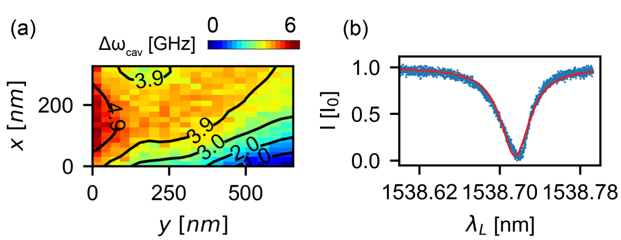

Fig. S5. Static and dynamic cavity heating. (a) Cavity heating induced by the tweezer field at different positions: the resonance is shifted by up to 5 GHz, while the shape and the width of the cavity response function remain unaffected. This map was taken during the scan in Fig. 2(b) in the main text. (b) Cavity heating induced by the intra-cavity field causes an asymmetry in the cavity response function. Above a certain threshold, the pump will cause dynamic instability of the cavity.

7. TRAPPING DISTANCE SIMULATION

As shown in Thompson *et al.* [7], the lattice formation, particularly the trapping locations with respect to the phtonic crystal's surface are defined by the thickness of the slab L:

$$z_i = -\frac{\phi}{4\pi}\lambda_{trap} + i\frac{\lambda_{trap}}{2}, \quad i = 0, 1, 2, ... \tag{S12}$$

with

$$\phi = \tan^{-1}\left(\frac{2n\cos(nkL)}{(1+n^2)\sin(nkL)}\right), \tag{S13}$$

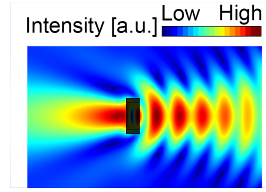

Fig. S6. Optical lattice. FEM simulation of the trap formation from the reflection of the tweezer light focused from the left on to the photonic crystal cavity (dark shaded area).

where $k = 2\pi/\lambda_{trap}$ is the optical wavevector and n the refactive index in silicon nitride. The measured thickness of our photonic crystal cavity is 310 nm, corresponding to $z_0 \sim 380$ nm. With a particle size of $r \sim 70$ nm, the surface-to-surface distance is $d_0 = z_0 - r \sim 310$ nm. Fig. S7 shows how, by reducing the cavity thickness to about 200 nm, the trapping position can be reduced to $z_0 \sim 220$ nm, corresponding to a surface-to-surface distance of $d_0 \sim 150$ nm.

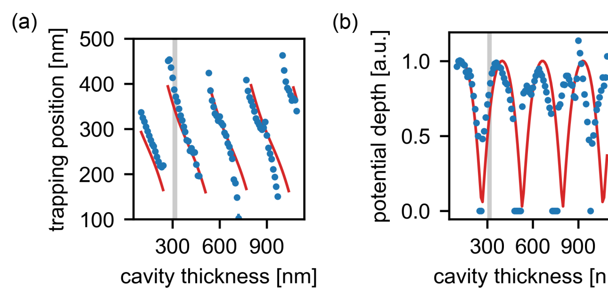

Fig. S7. Trap position simulation. (a) FEM simulation of the trapping position z_0 as a function of the cavity thickness. (b) Potential depth simulation as a function of the cavity thickness. Red solid lines show the theoretical expected value considering a plane incident wave. Gray shaded areas indicate our experimental conditions: thickness of 310nm, measured by SEM imaging.

8. CAVITY FIELD SIMULATION

The design of the photonic crystal cavity is based on finite element method (FEM) simulation. This also allows us to predict the amount of evanescent field and optimize the optomechanical coupling. For a qualitative understanding, we use a simple model of the cavity field as described in the following equation:

$$E^*E = E_0^2 e^{-\frac{y^2}{2\sigma_y}} e^{-\frac{x^2}{2\sigma_x}} e^{-\beta\sqrt{x^2+z^2}} \sin^2\left(\frac{2\pi}{\lambda}y\right). \tag{S14}$$

This model considers a standing wave with an intensity oscillation period of $\lambda/2$, Gaussian mode confinement in all directions (parameterized by σ_x and σ_y) inside the material and exponential evanescent field decay (parameterized by β) outside. We note that it does not account for the details of the photonic structure, only the dominant mode shape. Polarization and surface scattering are not considered as well. Close to the cavity axis (y axis), our model agrees well with the simulation (blue line in Fig. S8(c)). However, as one moves away from the center of the cavity, surface effects give rise to a more complex x dependence, reducing the the contrast of the field oscillations as

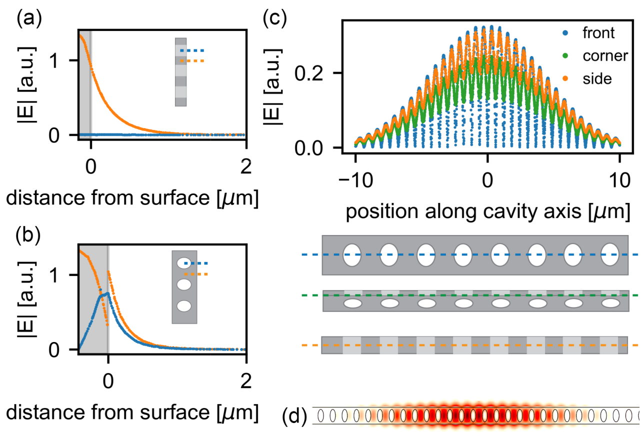

Fig. S8. FEM simulation of the cavity field. (a) Depicted is the cavity field as a function of a distance from the cavity surface moving away from its wide side, in correspondence of a hole (blue) or of the matter region (orange). The shaded area indicates the cavity extension. (b) Cavity field simulation as a function of distance from its narrow side in correspondence of a hole (blue) or matter (orange). (c) Simulation of the evanescent cavity field evaluated at 250 nm distance from the surface, and in front of the cavity (blue), at a corner (green) and at the side of the cavity (orange). Whenever one moves away from the cavity axis, the contrast of the oscillation is reduced and the field never vanishes. (d) Heat map of the simulated cavity field intensity.

shown in FEM simulation (Fig. S8). Nevertheless, one can derive single-photon optomechanical couplings for all three spatial mechanical modes from the model:

$$g_0^z(y) \propto |\partial_z E^* E| \propto \left|1 - \cos\left(2\frac{2\pi}{\lambda}y\right)\right|, \tag{S15}$$

$$g_0^y(y) \propto |\partial_y E^* E| \propto \left|\sin\left(2\frac{2\pi}{\lambda}y\right)\right|, \tag{S16}$$

$$g_0^x(y) \propto |\partial_x E^* E| \propto \left|1 - \cos\left(2\frac{2\pi}{\lambda}y\right)\right|. \tag{S17}$$

The deduced equations show qualitative agreements to the measurements shown in Fig. 2(b) in the main text. For instance, Eq. (S16) correctly predicts the shape of the modulation presented in the measured $g_0^y(y)$. Eq. (S15) and Eq. (S17) also capture the overall sinusoidal modulations in the measured data although they fail to predict the existence of non-zero offsets. These non-vanishing couplings are due to the fact that the particle is placed off from the cavity axis, which already led to the deviation of the model from the simulation in Fig. S8(c).

9. OPTOMECHANICAL COUPLING SIMULATION

A study of the expected coupling was carried out by FEM simulation in a static fashion. The expected cavity resonances were evaluated by placing a 75 nm radius nanopaticle at a given distance from the cavity surface. Simulations have been run at different distances both on the side and in front of the cavity. The result is fitted to an exponential decay of the cavity field. Assuming small particle displacements, the optomechanical coupling can be estimated in the linearized case:

$$G = \frac{\partial \omega_{cav}}{\partial z}\bigg|_{z=d} + \mathcal{O}(\delta\omega_{cav}^2). \tag{S18}$$

At a distance of $d = z_0 - r \sim 310$ nm, expected optomechanical couplings are 11 MHz/nm and 7 MHz/nm respectively for the case of the particle in front and on the side of the cavity (Fig. S9). The measured value (3.6 MHz/nm; see Fig. 2(b) in the main text) are lower than the simulation result, and can be explained by the fact that measurements were made slightly off the cavity axis as discussed previously.

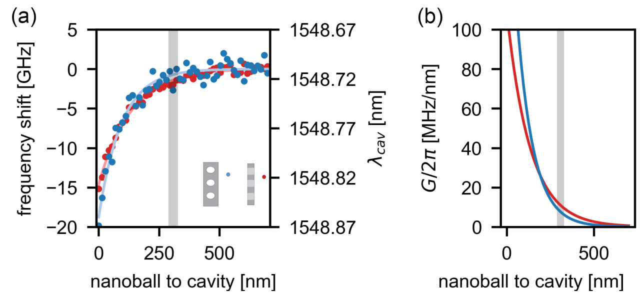

Fig. S9. Optomechanical frequency shift simulation. (a) FEM simulation of the cavity frequency shift as a function of the particle surface to cavity surface distance. The plot shows simulation results for the case of the particle in front (red) and on the side (blue) of the cavity. A gray shaded area indicates our experimental conditions: trapping at $z_0 \sim 380$ nm results in surface-to-surface distance of $d_0 \sim 310$ nm. An exponential decay follows the evanescent filed amplitude. (b) An estimated frequency shift per displacement as a function of d.

REFERENCES

1. M. J. Burek, C. Meuwly, R. E. Evans, M. K. Bhaskar, A. Sipahigil, S. Meesala, B. Machielse, D. D. Sukachev, C. T. Nguyen, J. L. Pacheco, E. Bielejec, M. D. Lukin, and M. Lončar, "Fiber-coupled diamond quantum nanophotonic interface," Phys. Rev. Appl. **8**, 024026 (2017).
2. R. Diehl, E. Hebestreit, R. Reimann, F. Tebbenjohanns, M. Frimmer, and L. Novotny, "Optical levitation and feedback cooling of a nanoparticle at subwavelength distances from a membrane," Phys. Rev. A **98**, 013851 (2018).
3. V. Jain, J. Gieseler, C. Moritz, C. Dellago, R. Quidant, and L. Novotny, "Direct measurement of photon recoil from a levitated nanoparticle," Phys. Rev. Lett. **116**, 243601 (2016).
4. M. R. Vanner, J. Hofer, G. D. Cole, and M. Aspelmeyer, "Cooling-by-measurement and mechanical state tomography via pulsed optomechanics," Nat. Commun. **4**, 2295 (2013).
5. M. Aspelmeyer, T. J. Kippenberg, and F. Marquardt, "Cavity optomechanics," Rev. Mod. Phys. **86**, 1391–1452 (2014).
6. H. Paul, "Shot noise in photodetectors and vacuum fluctuations," J. Mod. Opt. **35**, 1225–1235 (1988).
7. J. D. Thompson, T. G. Tiecke, N. P. de Leon, J. Feist, A. V. Akimov, M. Gullans, A. S. Zibrov, V. Vuletić, and M. D. Lukin, "Coupling a single trapped atom to a nanoscale optical cavity," Science. **340**, 1202–1205 (2013).